

Tuning of Atomic Layer Deposition Pulse Time through Physics-Informed Bayesian Active Learning

Pouyan Navabi¹ and Christos G. Takoudis^{1,2,3}

¹*Department of Chemistry, University of Illinois Chicago, Chicago, Illinois, 60607, USA*

²*Department of Biomedical Engineering, University of Illinois Chicago, Chicago, Illinois, 60607, USA*

³*Department of Chemical Engineering, University of Illinois Chicago, Chicago, Illinois, 60607, USA*

(*Electronic mail: takoudis@uic.edu)

(Dated: 24 February 2026)

Atomic Layer Deposition (ALD) process development is often hindered by time-consuming and precursor-intensive tuning cycles required to identify saturation conditions. We introduce a physics-informed Bayesian Active Learning (BAL) framework that autonomously tunes precursor pulse times by integrating a Langmuir adsorption model directly into the Gaussian Process (GP) kernel. A key innovation is a two-stage parameter estimation strategy that decouples noise filtering from physical parameter extraction: the GP first smooths noisy data through standard prediction, then Langmuir parameters are fitted to the noise-filtered GP predictions. This approach effectively separates signal from experimental noise. We evaluate the framework against a standard data-driven GP across four simulated regimes, demonstrating convergence within five iterations, up to fourfold improvement in prediction accuracy, and two to fourfold reduction in precursor usage. Experimental validation using TiO₂ deposition via Tetrakisdimethylamido Titanium (TDMAT) and ozone confirms that the physics-informed model accurately identifies saturation times for high-coverage targets ($\geq 95\%$), with observed deviations at lower saturation levels providing valuable insight into non-ideal desorption behaviors.

I. INTRODUCTION

Atomic layer deposition (ALD) is a vapor-phase thin film deposition technique that operates as a specialized form of chemical vapor deposition (CVD).¹ Unlike CVD, where reactants and co-reactants are introduced simultaneously, ALD relies on sequential, self-limiting surface reactions. A typical ALD cycle comprises four consecutive steps: (1) pulsing the precursor into the reaction chamber, (2) purging with an inert carrier gas, (3) introducing the co-reactant, and (4) performing a final purge. This sequence enables precise control of film thickness and conformality at the atomic scale.

Depositing materials one atomic layer at a time was initially a specialized task for the semiconductor industry,²⁻⁴ but it has evolved into a fundamental tool for modern manufacturing. Today, ALD is critical across many fields because it solves a unique challenge: coating complex, deep structures with a precision that other methods simply cannot match. From improving the efficiency of solar cells⁵⁻⁷ to encapsulating biomedical implants,⁸ the self-limiting nature of ALD provides a level of consistency that is essential for high-performance devices. Yet, as these applications expand, there is a growing need to make the process more efficient, specifically by minimizing waste⁹ and optimizing how quickly saturation is achieved.

Traditionally, determining this optimal saturation point is a resource-intensive task. It often requires extensive trial-and-error experimental campaigns that consume significant precursor material and machine time. As process complexity increases, these manual optimization methods become a bottleneck. To address this, data-driven approaches are emerging as a powerful alternative.¹⁰ Machine learning algorithms can analyze in situ data to predict saturation behavior with high

accuracy, significantly reducing the time and cost required to develop new ALD recipes.¹¹

Multiple process parameters critically influence the efficiency and quality of ALD growth.¹ The substrate temperature must be sufficiently high to activate surface reactions and prevent precursor condensation, yet low enough to avoid thermal decomposition. The precursor canister temperature determines vapor pressure and stability, while chamber pressure and carrier gas flow rate affect film uniformity, growth dynamics, and conformality. Another critical set of parameters includes the pulse and purge durations for both precursor and co-reactant, as these directly control material deposition and film growth per cycle. Tuning these parameters is therefore essential to achieve saturated surface reactions efficiently, minimize precursor waste, and ensure reproducible film quality.

Recent studies have highlighted the potential of machine learning to enhance ALD process development.¹⁰ Methods such as neural networks¹²⁻¹⁴ and Bayesian optimization (BO)¹⁵⁻¹⁷ have been applied to both computational and experimental workflows to extract saturation times, refine pulse sequences, and minimize experimental effort. In computational studies, particularly those coupling machine learning with computational fluid dynamics (CFD), these models have been used to predict surface coverage dynamics and identify optimal process parameters.¹⁸ Experimentally, Bayesian frameworks have been employed to iteratively suggest new process conditions to minimize defects, effectively reducing the number of required experiments.^{15,19} Paulson et al. developed a data-driven Bayesian framework for optimizing pulse and purge times using simulated datasets for Al₂O₃, TiO₂, and W,¹⁷ while more recent efforts toward closed-loop optimization have combined in situ characterization with machine

learning models. For instance, neural networks have been integrated with in situ quartz crystal microbalance (QCM) measurements and BO to enable real-time optimization of precursor exposure.²⁰

However, these approaches typically rely on reaction-specific trained models that must be developed and parameterized for each chemistry. Moreover, neural network-based approaches often function as digital twins or supervisory systems for the experimental setup, requiring simultaneous implementation of both the model and the control system. While effective, such architectures increase complexity and limit generalizability to new precursors or deposition chemistries. Unlike the approach of Paulson et al., which required reaction-specific trained models, a more flexible framework that balances physical insight with data-driven learning could potentially accelerate ALD process development across diverse material systems.

Recent advances in optimization for physical systems have focused on transitioning from black-box to grey-box Bayesian approaches that incorporate domain-specific physical relationships. Physics-informed BO integrates physics-infused kernels into Gaussian process (GP) surrogate models, enabling the framework to leverage both statistical and physical information during exploration.²¹ This strategy has proven effective across diverse applications. In materials design, physics-informed kernels enabled data-efficient identification of optimal NiTi shape memory alloy processing parameters to maximize transformation temperature.²² In computational chemistry, GP regression combined with BO reconstructed free-energy functions from molecular dynamics trajectories, propagating statistical uncertainty to accurately calculate phase diagrams for systems such as lithium across varying temperatures and pressures,²³ and in conformational analysis, a torsion-potential-based kernel with a specialized acquisition function successfully recovered previously missed low-energy molecular conformations in 40% of tested biologically relevant molecules.²⁴ These examples demonstrate that embedding physical structure into the learning framework substantially improves sample efficiency and extrapolation capability compared to purely data-driven approaches.

In this study, we present a physics-informed Bayesian active learning (BAL) framework for tuning precursor pulse duration in ALD using an adsorption model based on the Langmuir isotherm. The key methodological innovation is a two-stage parameter estimation strategy. Instead of fitting the Langmuir model directly to sparse, noisy observations, which often yields unstable parameters, we leverage smoothing capabilities of the GP by first generating dense, noise-free predictions from the GP, then fitting the Langmuir parameters to these smoothed predictions. This provides substantially more stable and robust parameter estimates while naturally filtering measurement noise.

We systematically test our physics-informed active learning framework in four simulated regimes: (i) **fast saturation**, where the optimal pulse to reach the target saturation falls near the lower limit of the search window; (ii) **moderate saturation**, where it falls near the upper limit; (iii) **slow saturation**, where it extends beyond the upper limit, requiring extrapo-

lation; and (iv) **high noise**, where the data is influenced by elevated noise conditions. Finally, we validate the framework experimentally using in situ spectroscopic ellipsometry (SE) feedback for the ALD of TiO₂. By combining in situ SE feedback with this physics-informed BAL approach, the system autonomously identifies tuned pulse times with high accuracy, reduces precursor consumption, and accelerates process development.

II. METHODOLOGY

A. Adsorption Kinetics Models

1. Langmuir Isotherm Model

We employ a Langmuir isotherm model^{25,26} to represent the adsorption behavior of precursors during ALD with only exposure time as the effective parameter. The rationale for this approach is that in typical ALD processes, the substrate temperature is determined by the chemical thermodynamics of the precursor and substrate, as well as considerations of precursor and substrate stability and the resulting film quality. The canister temperature is set based on the physical properties of the precursor to ensure adequate vapor pressure. Flow rate and chamber pressure are defined by instrument design and growth dynamics. In most ALD cases, these parameters are well-established for a given process, and tuning efforts focus primarily on pulse and purge times.

For chemical adsorption in ALD, the surface reaction can be represented as:



where precursor A from the gas phase binds to available surface sites S \cdot , forming the adsorbed species AS. Based on this mechanism, we define the kinetics using a modified Langmuir adsorption model. In a real experimental environment, desorption during the purge step is non-negligible.²⁷ Therefore, the growth rate $y(x)$ as a function of exposure time x is more accurately described as:

$$y(x) = \frac{G_{\max}Kx}{1 + Kx} - D(x) \quad (2)$$

where G_{\max} is the maximum surface coverage, K is the equilibrium constant, and $D(x)$ accounts for material desorption. Ideally, $D(x)$ is negligible compared to the adsorption term, and our experimental protocols aim to minimize it.

In our simulations, we assume ideal behavior where $D(x) \approx 0$, effectively setting:

$$y(x) = \frac{G_{\max}Kx}{1 + Kx} \quad (3)$$

However, in our experimental validation, we implement a specific protocol to address the desorption term. We employ

an extended 600-second purge and measure the thickness after a sequence of four consecutive pulses. The extended purge minimizes the magnitude of the desorption effect for each new parameter set. Furthermore, since typical ALD recipes do not utilize 600-second purges, the prior four-pulse sequence ensures that $D(x)$ effectively becomes a constant offset associated only with the current parameter x being evaluated. This protocol helps isolate the adsorption kinetics necessary for the learning algorithm. In our simulations, the true parameters ($K_{\text{true}}, G_{\text{true}}$) are hidden from the physics-informed BAL framework and used only to generate observations.

2. Realistic Noise Model

To simulate realistic experimental limitations, we implement a two-component Gaussian noise model. The first source of uncertainty arises from the thickness measurement method and represents constant absolute measurement noise:

$$\sigma_{y,\text{direct}} = \sigma_{y,\text{abs}} \quad (4)$$

where $\sigma_{y,\text{abs}}$ represents constant absolute detector noise arising from detector resolution, readout noise, and environmental fluctuations.

The second source of noise originates from timing precision limitations of ALD valves. This timing uncertainty propagates through the Langmuir model derivative:

$$\frac{dy}{dx} = \frac{G_{\text{max}}K}{(1+Kx)^2} \quad (5)$$

The contribution of x -uncertainty to the observed y -noise is obtained from:

$$\sigma_{y,\text{timing}} = \left| \frac{dy}{dx} \right| \times \sigma_{x,\text{abs}} = \frac{G_{\text{max}}K}{(1+Kx)^2} \times \sigma_{x,\text{abs}} \quad (6)$$

where $\sigma_{x,\text{abs}}$ represents constant absolute timing precision. This creates heteroscedastic (input-dependent) noise that is larger at small x where the Langmuir curve has a steeper slope, naturally creating noise that decreases with increasing exposure time.

The total measurement uncertainty combines both independent sources in quadrature:

$$\sigma_{\text{total}}(x) = \sqrt{\sigma_{y,\text{direct}}^2 + \sigma_{y,\text{timing}}^2} \quad (7)$$

Observations are then drawn with Gaussian probability as:

$$y_{\text{obs}}(x) = y(x) + \mathcal{N}(0, \sigma_{\text{total}}^2(x)) \quad (8)$$

This noise model is physically motivated by the causality of the experiment where x is the controlled variable and y is the measured variable. Both sources of uncertainty manifest as scatter in the observed y -values.

B. Physics-Informed Bayesian Active Learning

The learning framework serves as a sequential design strategy to efficiently characterize expensive-to-evaluate functions. We employ GP regression to construct a surrogate model of the saturation curve. While standard GP regression is well-documented^{28,29}, our implementation introduces two domain-specific modifications: a physics-informed covariance kernel and a two-stage parameter estimation strategy. All GP regression algorithms and BAL procedures were implemented using Python modules, including scikit-learn³⁰ for GP regression, scipy³¹ for optimization routines, and numpy for numerical computations.

1. Gaussian Process Regression

We model the growth rate $f(x)$ as a Gaussian Process specified by a zero mean function²⁸ and a covariance kernel $k(x, x')$. Given a set of n observations $D = \{(x_i, y_i)\}_{i=1}^n$, the posterior predictive distribution at a new test point x_* is Gaussian $\mathcal{N}(\mu(x_*), \sigma^2(x_*))$, where the mean $\mu(x_*)$ and variance $\sigma^2(x_*)$ are calculated analytically. The 95% confidence interval (CI) represents the region within ± 1.96 standard deviations of the posterior mean, capturing the uncertainty in the GP predictions. In our active learning framework, we utilize the posterior variance $\sigma^2(x_*)$ to drive exploration via uncertainty sampling, selecting the next sampling point as $x_{\text{next}} = \arg \max_x \sigma^2(x)$.

2. Kernel Strategies

The choice of covariance function (kernel) $k(x, x')$ encodes our prior assumptions about the smoothness and structure of the underlying function. We compare two GP kernel strategies:

- **Physics-informed Matérn kernel ($\nu = 2.5$):** integrates a Langmuir transformation into the GP kernel with adaptive physics parameters.
- **Pure Matérn kernel ($\nu = 2.5$):** purely statistical GP with no embedded physics.

We employ the Matérn kernel rather than other common kernels (such as the squared exponential or radial basis function) because it provides greater flexibility in modeling function smoothness through the parameter ν . The Matérn class encompasses a broad family of covariance functions, and the choice of $\nu = 2.5$ represents a balance between smoothness and flexibility.³² This value corresponds to functions that are twice differentiable, which aligns well with the expected behavior of adsorption isotherms. Additionally, $\nu = 2.5$ has been found empirically to perform well for physical systems exhibiting smooth but not infinitely differentiable behavior, making it particularly suitable for capturing the characteristic saturation curve of Langmuir kinetics while remaining robust to experimental noise.

a. Physics-Informed Matérn Kernel The physics-informed kernel projects the input x through a Langmuir-inspired transformation:

$$\phi(x) = \frac{G_{\text{phys}} K_{\text{phys}} x}{1 + K_{\text{phys}} x} \quad (9)$$

The correlation between x_i and x_j is defined using the Matérn covariance function:

$$k_{\text{phys}}(x_i, x_j) = \frac{2^{1-\nu}}{\Gamma(\nu)} \times (\sqrt{2\nu}r)^{\nu} \times K_{\nu}(\sqrt{2\nu}r) \quad (10)$$

where $r = |\phi(x_i) - \phi(x_j)|/\ell$, ℓ is the correlation length scale (a hyperparameter that controls the distance over which function values are correlated), Γ is the gamma function, and K_{ν} is the modified Bessel function of the second kind. The length scale ℓ is optimized during GP training by maximizing the marginal log-likelihood of the observed data, allowing the model to automatically determine the appropriate correlation structure from the measurements.

A critical innovation in this framework is the estimation of the adaptive parameters K_{phys} and G_{phys} . Direct fitting of the Langmuir model to sparse, noisy ALD data often yields unstable parameters. Instead, we adopt a hierarchical two-stage approach:

1. **Smooth:** The GP is trained on the available noisy data (x, y_{obs}) , acting as a sophisticated noise filter that handles heteroscedastic uncertainty.
2. **Fit:** We generate dense, noise-free predictions from the GP posterior mean on a fine grid and fit the Langmuir parameters $(K_{\text{phys}}, G_{\text{phys}})$ to this smoothed curve.

This decouples noise rejection (handled by the GP) from physical interpretation (handled by the Langmuir fit), resulting in significantly more robust convergence during the early stages of the active learning process.

b. Pure Matérn Kernel A purely data-driven model without physics transformation is defined as:

$$k_{\text{Matérn}}(x_i, x_j) = \frac{2^{1-\nu}}{\Gamma(\nu)} \times (\sqrt{2\nu}r')^{\nu} \times K_{\nu}(\sqrt{2\nu}r') \quad (11)$$

where $r' = |x_i - x_j|/\ell$. The correlation length scale ℓ is likewise optimized by maximizing the marginal log-likelihood, providing the model with the flexibility to learn appropriate correlations directly from the data without incorporating domain-specific knowledge. This kernel serves as a baseline that relies solely on data smoothness assumptions without domain-specific structure.

3. Active Learning Workflow

The goal of our methodology is to identify the optimal data points that yield the best Langmuir fit (K and G_{max} values) and

TABLE I. Adjustable parameters for simulation and Bayesian learning models

Parameter	Description
<i>Simulation Parameters</i>	
K_{true}	True Langmuir equilibrium constant (1/s)
$G_{\text{max, true}}$	True maximum surface coverage (Å)
$\sigma_{y, \text{abs}}$	Absolute y-uncertainty (measurement noise, Å)
$\sigma_{x, \text{abs}}$	Absolute x-uncertainty (timing precision, s)
N_{MC}	Number of Monte Carlo runs
$N_{\text{iter, MC}}$	Iterations per Monte Carlo run
<i>Bayesian Learning Parameters</i>	
N_{iter}	Number of active learning iterations
N_{survey}	Initial Latin Hypercube Sampling survey points
x_{min}	Exploration window minimum (s)
x_{max}	Exploration window maximum (s)
ν	Matérn smoothness parameter
s_{target}	Target saturation fraction

then use this optimized fit to predict the targeted saturation. This methodology ensures that saturation can be accurately predicted even when the targeted saturation falls outside the exploration window. The adjustable parameters for the active learning framework are provided in Table I.

The iterative exploration procedure, illustrated in Figure 1, follows these steps:

1. **Initialize:** Latin Hypercube Sampling (LHS) generates N_{survey} random points in the exploration window $[x_{\text{min}}, x_{\text{max}}]$ to initiate BAL parameters. LHS ensures better space-filling coverage than simple random sampling.
2. **Train GP:** Fit the GP to observed data (x, y_{obs}) with noise variance $\sigma_{\text{total}}^2(x)$.
3. **Predict:** Compute the posterior mean $\mu(x)$ and standard deviation $\sigma(x)$ over a dense grid.
4. **Explore:** Choose the next sampling point as $x_{\text{next}} = \arg \max_x \sigma^2(x)$, implementing a pure exploration (maximum uncertainty) acquisition function. Note that while this framework utilizes the machinery of BO, it functions as a BAL protocol; the objective is not to maximize the growth rate itself, but to minimize the uncertainty in the model parameters (K, G_{max}) to accurately predict the saturation behavior.
5. **Sample:** Measure new data y_{next} from the true Langmuir model with noise according to Equation 8.
6. **Update:** Generate dense GP predictions over a high-resolution grid (1000 points per unit interval). Fit the Langmuir model to these GP mean predictions to obtain updated parameter estimates. For the physics-informed kernel, update $(K_{\text{phys}}, G_{\text{phys}})$ using these GP-fitted values. Calculate cumulative exploration cost ($\sum x_i$) and relative error in predicting x_{sat} for target saturation.
7. **Repeat:** Continue until N_{iter} iterations are reached.

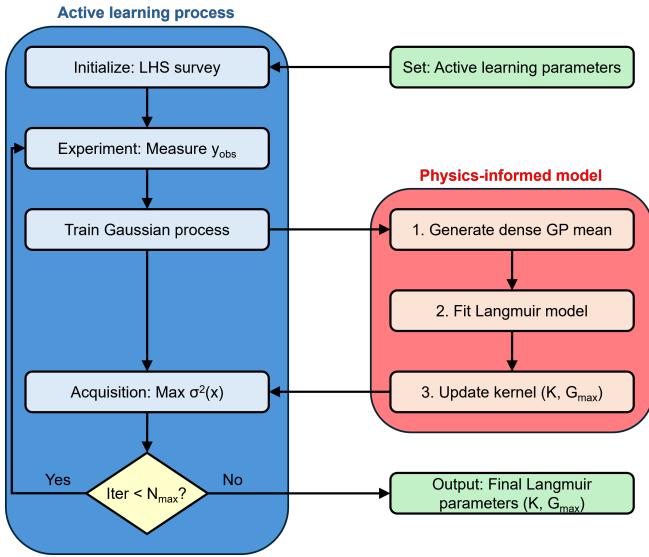


FIG. 1. Flowchart of the Physics-Informed Bayesian Active Learning framework. The red highlighted section details the novel two-stage parameter estimation strategy, where physical parameters are extracted from the smoothed GP surrogate to ensure robustness against experimental noise.

After the specified number of iterations, the predicted dose time required to reach the targeted saturation is given by:

$$x_{\text{sat},t} = \frac{s_{\text{target}}}{K_t(1 - s_{\text{target}})} \quad (12)$$

The true value can be calculated from:

$$x_{\text{sat},\text{true}} = \frac{s_{\text{target}}}{K_{\text{true}}(1 - s_{\text{target}})} \quad (13)$$

To evaluate the accuracy of the predicted value, the relative error is calculated as:

$$\text{Error}_{\text{sat}} = 100 \times \frac{|x_{\text{sat},t} - x_{\text{sat},\text{true}}|}{x_{\text{sat},\text{true}}} \quad (\%) \quad (14)$$

Cumulative exploration cost is defined as:

$$C(n) = \sum_{i=1}^n x_i \quad (15)$$

where n is the iteration number. This metric quantifies the total experimental resource consumption (e.g., total exposure time), serving as a proxy for precursor usage efficiency.

III. SIMULATION RESULTS

We evaluate model performance across four distinct simulated scenarios: (i) **fast saturation**, where the optimal pulse

to reach the target saturation falls near the lower limit of the search window; (ii) **moderate saturation**, where the optimal pulse falls near the upper limit; (iii) **slow saturation**, where the optimal pulse extends beyond the upper limit, requiring extrapolation; (iv) **high noise**, where the measurements have intensified uncertainties. To model scenarios (i)–(iii), we maintain constant values for $G_{\text{max},\text{true}} = 1.0$, $x_{\text{min}} = 0.005$, and $x_{\text{max}} = 10.0$ while varying K_{true} to position the saturation point within the respective regions. Across these scenarios, we introduce realistic experimental noise with $\sigma_{y,\text{abs}} = 0.05$ and $\sigma_{x,\text{abs}} = 0.005$, and initialize each run with $N_{\text{survey}} = 5$ LHS survey scans. For scenario (iv), we used the parameters for scenario (ii) while adjusted $\sigma_{y,\text{abs}} = 0.2$ and $\sigma_{x,\text{abs}} = 0.01$. The target saturation was set to 99% of G_{max} for all simulations. We perform 20 iterations to demonstrate the capability of our model to achieve accurate predictions with relatively few iterations.

A. Fast Saturation

In this regime, we set $K_{\text{true}} = 100$ to evaluate model performance when saturation occurs rapidly within the lower portion of the search window. Figure 2 compares the exploration behavior of the two kernel strategies over 20 iterations. The physics-informed Matérn kernel demonstrates a marked preference for sampling regions where the adsorption isotherm exhibits a steeper slope, corresponding to the most informative portion of the Langmuir curve. This targeted exploration contrasts sharply with the pure Matérn kernel, which bases its sampling decisions solely on GP uncertainty without incorporating knowledge of the underlying adsorption kinetics.

To evaluate the statistical robustness and efficiency of the physics-informed model, we performed 100 Monte Carlo simulations with different random error realizations, removing statistical outliers using the Interquartile Range (IQR) method. The results presented in Figure 3 demonstrate that the physics-informed kernel predicts the 99% saturation time after 20 iterations with a mean error of $18.7 \pm 13.5\%$, compared to $70.3 \pm 53.2\%$ for the pure Matérn kernel, a nearly fourfold improvement in prediction accuracy. Furthermore, the cost evaluation reveals more than fourfold improvement in precursor usage efficiency, demonstrating substantial resource savings in addition to enhanced predictive performance.

B. Moderate Saturation

For the moderate saturation regime, we set $K_{\text{true}} = 10$ to position the saturation point near the upper limit of the search window. Figure 4 illustrates the exploration behavior of the two kernels over 20 iterations. In this scenario, the physics-informed Matérn kernel demonstrates a more distributed exploration pattern compared to the fast saturation case. While the kernel still leverages the embedded Langmuir structure to guide sampling, exploration of the high-slope region is less intensive, as the saturation curve extends further into the search domain. This behavior reflects the adaptive nature of

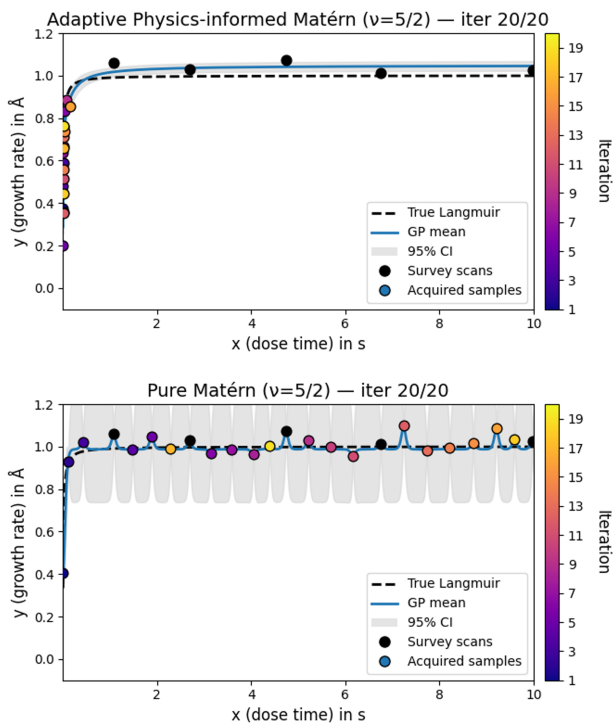


FIG. 2. Exploration behavior comparison for fast saturation regime ($K_{\text{true}} = 100$) over 20 iterations. Physics-informed Matérn kernel (top) prioritizes high-slope regions of the Langmuir curve, while pure Matérn kernel (bottom) explores based solely on GP uncertainty. Gray shaded regions represent 95% confidence intervals. Colors indicate iteration number.

the physics-informed approach, which adjusts its exploration strategy based on the learned parameters (K_{phys} , G_{phys}) as they converge toward the true values.

Statistical analysis over 100 Monte Carlo simulations reveals the continued advantage of the physics-informed kernel in this regime. As shown in Figure 5, the physics-informed model predicts the 99% saturation time after 20 iterations with a mean error of $11.5 \pm 9.0\%$, compared to $53.3 \pm 30.7\%$ for the pure Matérn kernel. The cost analysis demonstrates approximately threefold improvement in precursor usage efficiency for the physics-informed approach relative to the pure Matérn kernel, highlighting significant resource savings even when saturation occurs at longer exposure times.

C. Slow Saturation

In the slow saturation regime, we set $K_{\text{true}} = 1$ to position the saturation point beyond the upper limit of the search window, requiring extrapolation from the explored region to predict the target saturation time. While this regime demonstrates the robustness of our framework for extrapolation and may prove useful for precursors with substantially low vapor pressure, it does not represent a typical application scenario. In standard ALD process development, practitioners select search windows that encompass the expected saturation range

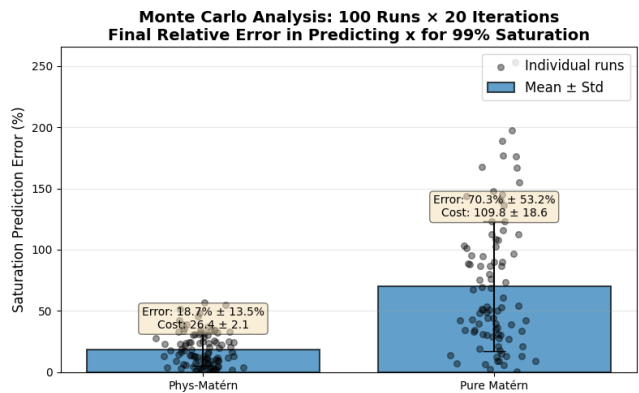


FIG. 3. Monte Carlo statistical analysis for fast saturation regime ($K_{\text{true}} = 100$) over 100 independent runs after 20 iterations. Left bar: physics-informed Matérn achieves $18.7 \pm 13.5\%$ error. Right bar: pure Matérn shows $70.3 \pm 53.2\%$ error. Physics-informed approach reduces precursor usage by approximately fourfold. Error bars represent mean \pm standard deviation after outlier removal via IQR method.

rather than targeting saturations far beyond the upper limit, as this would result in low-throughput processing. Figure 6 demonstrates the exploration behavior over 20 iterations. In this challenging scenario, the physics-informed Matérn kernel exhibits an even more distributed exploration pattern than observed in the moderate saturation case. The kernel spreads its sampling across a broader range of exposure times, attempting to capture the gradual approach toward saturation that extends beyond the predefined search boundary. This behavior contrasts with the more localized exploration strategies observed when saturation falls within the search window, reflecting the model's adaptation to the underlying kinetics.

Statistical analysis over 100 Monte Carlo simulations demonstrates that even in this extrapolation regime, the physics-informed kernel maintains an accuracy advantage over the pure Matérn approach. As illustrated in Figure 7, the physics-informed model predicts the 99% saturation time with a mean error of $9.2 \pm 6.2\%$, compared to $11.4 \pm 7.7\%$ for the pure Matérn kernel, representing approximately 20% improvement in prediction accuracy. This performance advantage is notable, indicating that the embedded physical structure provides meaningful guidance even when extrapolating beyond the explored region. Furthermore, the cost analysis reveals that the physics-informed approach maintains approximately twofold improvement in precursor usage efficiency, demonstrating dual advantages in both accuracy and resource consumption.

D. High Noise Regime

To evaluate the robustness of both kernel strategies under challenging experimental conditions, we conducted an additional analysis using substantially elevated noise levels. For this investigation, we employed the moderate saturation

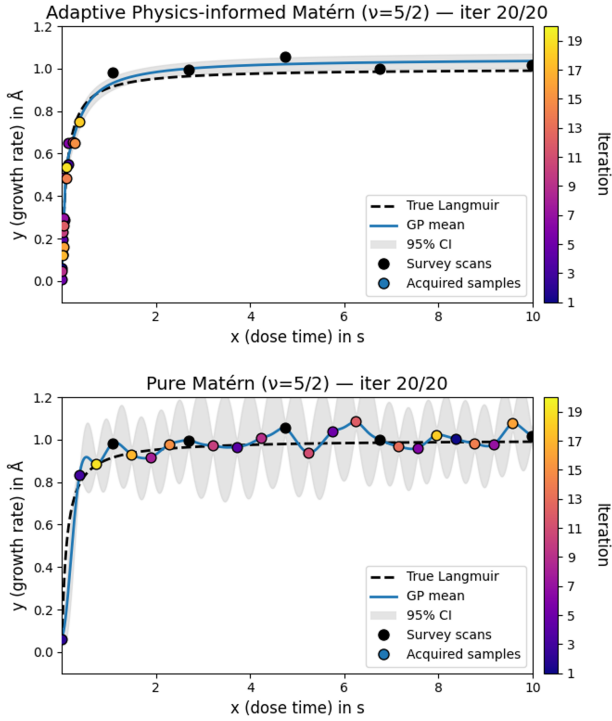


FIG. 4. Exploration behavior comparison for moderate saturation regime ($K_{\text{true}} = 10$) over 20 iterations. Physics-informed Matérn kernel (top) shows distributed exploration as saturation extends into the search domain. Pure Matérn kernel (bottom) explores based on GP uncertainty. Gray shaded regions represent 95% confidence intervals. Colors indicate iteration number.

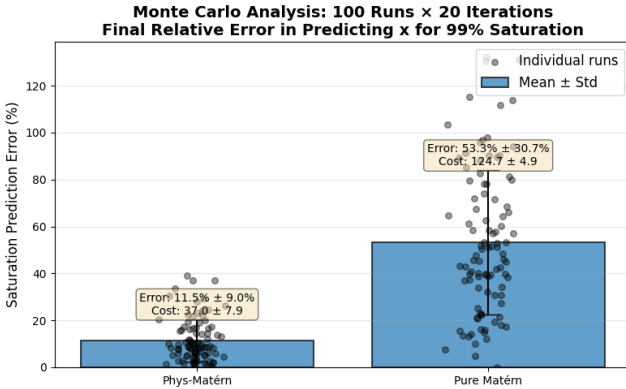


FIG. 5. Monte Carlo statistical analysis for moderate saturation regime ($K_{\text{true}} = 10$) over 100 independent runs after 20 iterations. Left bar: physics-informed Matérn achieves $11.5 \pm 9.0\%$ error. Right bar: pure Matérn shows $53.3 \pm 30.7\%$ error. Threefold reduction in precursor usage for physics-informed approach. Error bars represent mean \pm standard deviation after outlier removal via IQR method.

regime ($K_{\text{true}} = 10$), which provided the most favorable balance between exploration window coverage and extrapolation requirements in previous sections. The noise parameters were increased relative to the baseline simulations: $\sigma_{y,\text{abs}} = 0.2$ for measurement uncertainty and $\sigma_{x,\text{abs}} = 0.01$ for timing preci-

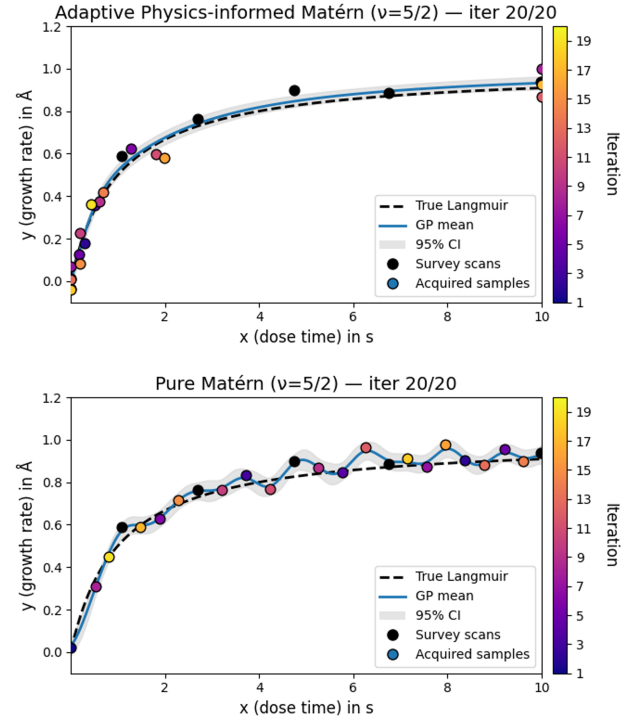


FIG. 6. Exploration behavior comparison for slow saturation regime ($K_{\text{true}} = 1$) over 20 iterations, where saturation lies beyond the search window. Physics-informed Matérn kernel (top) exhibits distributed exploration across broad exposure ranges. Pure Matérn kernel (bottom) shows similar widespread exploration. Gray shaded regions represent 95% confidence intervals. Colors indicate iteration number.

sion. These elevated noise levels represent scenarios where measurement equipment operates near its detection limits or where environmental fluctuations significantly impact data quality.

Figure 8 illustrates the exploration behavior under high noise conditions over 20 iterations. The substantially increased uncertainty manifests as greater scatter in the observed data points relative to the true Langmuir curve, reflecting the challenging measurement environment. Despite this heightened noise, the physics-informed Matérn kernel maintains its characteristic sampling strategy, continuing to prioritize regions where the adsorption isotherm exhibits steeper slopes. This behavior demonstrates the robustness of the physics-informed approach: even when individual measurements are significantly corrupted by noise, the embedded Langmuir structure guides the learner toward the most informative regions of the parameter space, where the signal-to-noise ratio for learning the underlying kinetics remains relatively favorable.

Statistical analysis over 100 Monte Carlo simulations reveals that the physics-informed kernel maintains a significant performance advantage even under these degraded measurement conditions. As shown in Figure 9, the physics-informed model predicts the 99% saturation time with a mean error of $25.1 \pm 18.5\%$, compared to $44.4 \pm 33.8\%$ for the pure

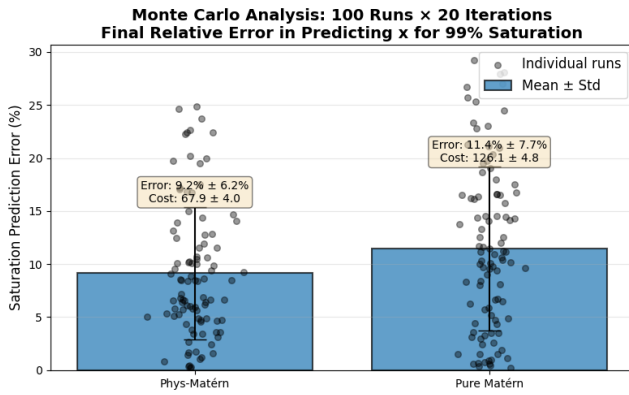


FIG. 7. Monte Carlo statistical analysis for slow saturation regime ($K_{\text{true}} = 1$) over 100 independent runs after 20 iterations. Left bar: physics-informed Matérn achieves $9.2 \pm 6.2\%$ error. Right bar: pure Matérn shows $11.4 \pm 7.7\%$ error. Twofold improvement in both prediction accuracy and precursor usage efficiency. Error bars represent mean \pm standard deviation after outlier removal via IQR method.

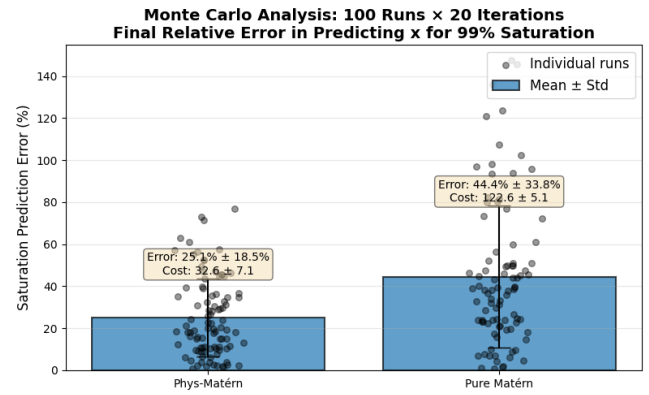


FIG. 9. Monte Carlo statistical analysis for high noise regime ($K_{\text{true}} = 10$) over 100 independent runs after 20 iterations. Left bar: physics-informed Matérn achieves $25.1 \pm 18.5\%$ error. Right bar: pure Matérn shows $44.4 \pm 33.8\%$ error. Nearly 75% improvement in prediction accuracy and fourfold improvement in precursor usage efficiency. Error bars represent mean \pm standard deviation after outlier removal via IQR method.

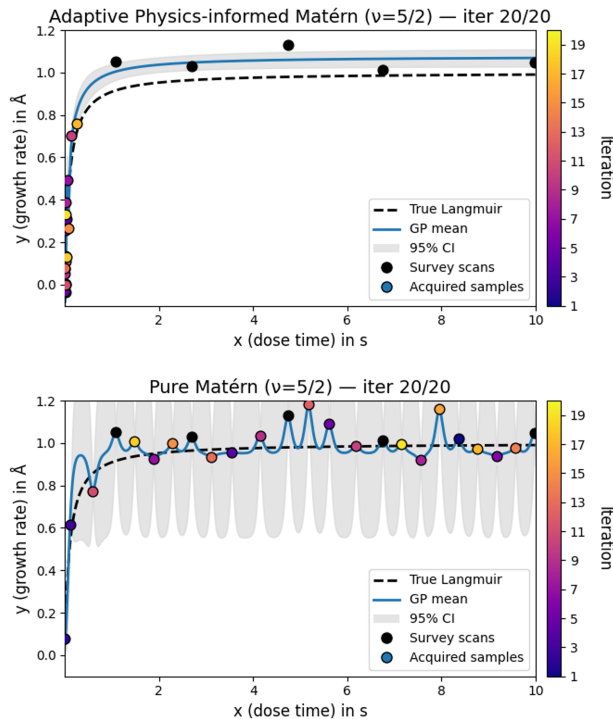


FIG. 8. Exploration behavior comparison under high noise conditions ($K_{\text{true}} = 10$, $\sigma_{y,\text{abs}} = 0.2$, $\sigma_{x,\text{abs}} = 0.01$) over 20 iterations. Physics-informed Matérn kernel (top) maintains focus on high-slope regions despite increased data scatter. Pure Matérn kernel (bottom) explores based on GP uncertainty. Elevated noise levels cause greater deviation from the true Langmuir curve (dashed line). Gray shaded regions represent 95% confidence intervals. Colors indicate iteration number.

Matérn kernel. While both models exhibit larger prediction errors than observed under nominal noise conditions, the physics-informed approach achieves approximately 75% improvement in accuracy relative to the pure statistical method. Moreover, the cost analysis continues to demonstrate approximately fourfold improvement in precursor usage efficiency, indicating that the physics-informed strategy not only produces more accurate predictions but also achieves this performance with more efficient resource utilization.

E. Convergence Analysis

To fully assess the learning efficiency of the proposed framework, we analyze the convergence behavior of the predicted saturation time across all four simulated regimes. Figure 10 summarizes these results. In the Fast Saturation regime ($K_{\text{true}} = 100$), the physics-informed model converges to the actual saturation value effectively after just five iterations (Figure 10a). In stark contrast, the pure Matérn kernel shows no meaningful improvement during these initial steps. This difference highlights that the incorporation of physical structure not only enhances initial predictions but also accelerates learning.

Similar rapid convergence is observed in the Moderate Saturation regime ($K_{\text{true}} = 10$), where the physics-informed model stabilizes near the true value by iteration five (Figure 10b), confirming that the advantage is robust to the location of the saturation point. In the Slow Saturation regime ($K_{\text{true}} = 1$), the framework demonstrates its most significant capability for extrapolation (Figure 10c). Even though the target saturation lies outside the search space, the physics-informed model predicts the correct saturation time with high accuracy after minimal iterations, whereas the pure Matérn kernel struggles to extrapolate during initial iterations.

TABLE II. Summary of performance over 20 iterations

Regime	Prediction Error (%)		Precursor Usage
	Phys-Matérn	Pure Matérn	Reduction Factor
Fast Saturation	18.7 ± 13.5	70.3 ± 53.2	~4×
Moderate Saturation	11.5 ± 9.0	53.3 ± 30.7	~3×
Slow Saturation	9.2 ± 6.2	11.4 ± 7.7	~2×
High Noise	25.1 ± 18.5	44.4 ± 33.8	~4×

Finally, in the High Noise regime, the convergence analysis (Figure 10d) demonstrates the efficacy of the two-stage parameter estimation strategy. Even with significant data scatter, the physics-informed model leverages the GP’s smoothing capabilities to filter high-frequency noise, allowing it to accurately predict the saturation time after just five iterations. The model successfully separates signal from noise by adhering to the physical constraints of the Langmuir isotherm.

Table II summarizes the performance metrics across all four regimes, highlighting the consistent efficiency gains and accuracy improvements offered by the physics-informed approach.

IV. EXPERIMENTAL VALIDATION

A. Experimental Setup

To validate our framework in a real experimental setting, we applied our physics-informed approach to predict the saturation time for Tetrakisdimethylamido Titanium (TDMAT) in TDMAT/O₃ ALD for TiO₂ deposition on silicon wafers using a commercial system (ALD-150LX, Kurt J. Lesker Company). The experimental parameters were as follows: substrate temperature of 150 °C (selected to avoid precursor decomposition while ensuring sufficient reactivity), chamber pressure of 1 Torr, TDMAT canister temperature of 50 °C, and precursor line heating to 100 °C to prevent condensation.

The pulse/purge sequence was defined as $(x : 30 : 1 : 15) \times 4 + (x : 30 : 1 : 600)$ where x represents the tuned TDMAT pulse time, followed by a 30-second Ar purge, a 1-second O₃ pulse (15% nominal concentration), and a final Ar purge. This sequence consists of four stabilization cycles with standard 15-second purges to reach equilibrium, followed by a fifth measurement cycle with an extended 600-second purge. Growth per cycle (GPC) was determined by measuring the thickness difference for a single pulse inserted after four consecutive pulses, specifically comparing measurements taken 15 seconds after the final purge and immediately before the fifth precursor pulse. This five-pulse protocol combined with the 600-second purge is critical for handling non-ideal desorption effects. The extended purge minimizes desorption between measurements, while the four-pulse conditioning ensures that any residual desorption appears as a reproducible offset rather than a time-varying artifact that would distort the Langmuir kinetics significantly. Thickness measurements were performed using in situ ellipsometry (FS-1EX, FilmSense) at a 70° incident angle with a predefined Si/SiO₂(native oxide)/TiO₂ optical model in the provided soft-

ware.

B. Experimental Results and Discussion

Using a modified experimental version of the code to get growth input directly from user, we conducted five survey scans followed by 10 BAL iterations. For the experimental runs, the search window was defined as 0.200–5.000 seconds. This lower bound (0.200 s) differs from the simulation lower bound (0.005 s) because the effect of the desorption term becomes significantly greater relative to the growth at very short pulse times. In this region, deviations from ideal Langmuir behavior increase, which can negatively affect the acquisition function and isotherm fitting and cause a significant deviation between GP fit and ideal Langmuir fit at the extreme lower end. By restricting the window to 0.200 s, we mitigate the influence of these desorption artifacts on the learning and prediction process.

Figure 11 shows the distribution of sampled points across iterations. Notably, after the initial survey scans, the Bayesian framework predominantly selected experimental points in two regions: the highly saturated regime (highest pulse time) and the steepest portion of the isotherm where uncertainty is greatest, while relying on survey scans for the mid-range. This sampling strategy is consistent with the behavior observed in simulations and reflects the physics-informed kernel’s bias toward informative regions. Figure 12 presents the experimental results and the evolution of K and G_{\max} values across iterations, demonstrating stable convergence of both physical parameters.

To assess the accuracy of the predicted saturation times, we evaluated the experimental growth at targeted saturation levels of 0.95, 0.90, 0.85, and 0.80 by using the final parameters obtained from BAL shown in Figure 12 and using Equation 12 to calculate respective pulse times. The results are summarized in Table III and visualized in Figure 13. The maximum growth per cycle (G_{\max}) was determined to be 0.045 nm, which matches reported growth for TDMAT/O₃ ALD in the literature.³³ The model accurately predicted the saturation time for the 0.95 saturation target (5.217 s), yielding a GPC of 0.0425 nm (0.6% error). However, as the targeted saturation decreased to lower values, the deviation between model predictions and experimental results increased. For the 0.90 target (2.471 s), the GPC was 0.0378 nm (6.8% error); for the 0.85 target (1.556 s), the GPC was 0.0345 nm (9.8% error); and for the 0.80 target (1.098 s), the GPC was 0.0313 nm (13.0% error).

We attribute this discrepancy to the desorption term $D(x)$ in Equation 2. While the extended 600-second purge minimizes this effect, it cannot be entirely eliminated, and its relative impact is more pronounced at lower surface coverages where the driving force for adsorption is lower. At high saturation levels (95%), the surface is nearly fully occupied, and non-ideal effects represent a small fraction of the total coverage. At lower saturation levels, however, fewer sites are occupied, and when a long pulse follows by a short pulse without extended purge, the same amount of continuous desorption results in a

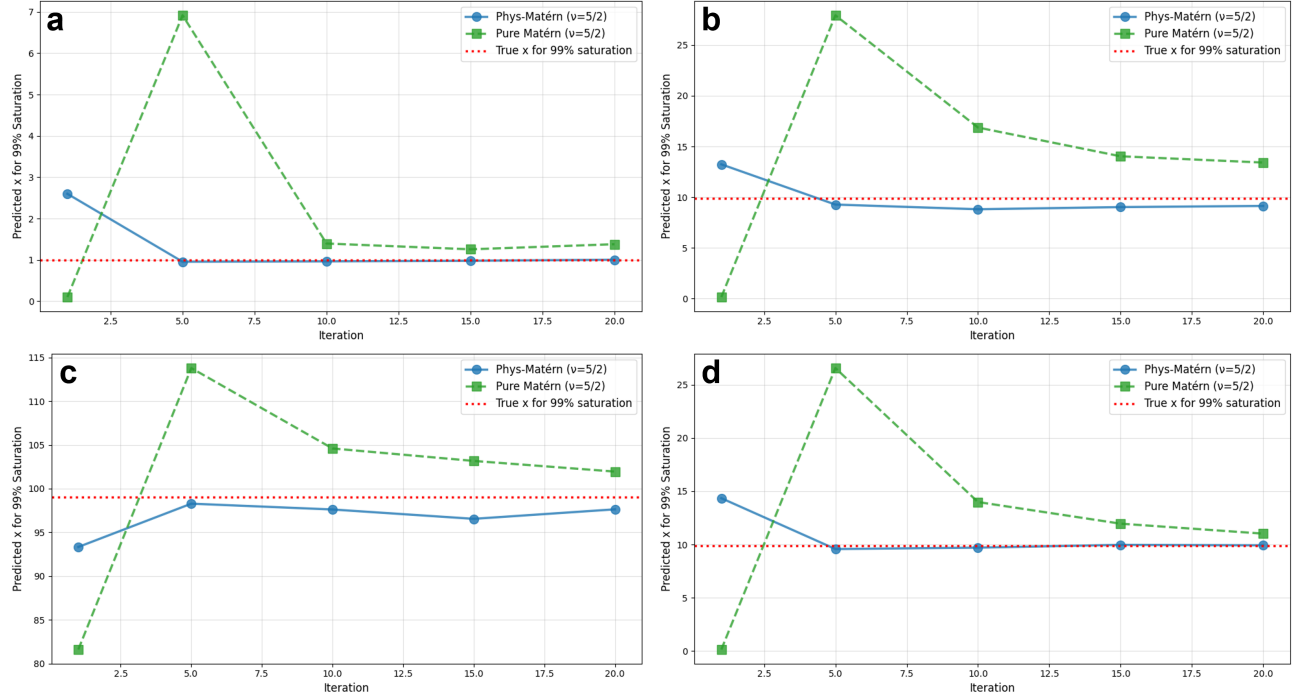


FIG. 10. Convergence analysis of the predicted saturation time across four simulated regimes, averaged over 100 Monte Carlo runs. (a) Fast Saturation ($K_{\text{true}} = 100$): The physics-informed model (solid blue) converges immediately, while the pure Matérn (dashed green) lags. (b) Moderate Saturation ($K_{\text{true}} = 10$): The physics-informed model stabilizes within five iterations. (c) Slow Saturation ($K_{\text{true}} = 1$): The physics-informed model successfully extrapolates to find the saturation point outside the search window. (d) High Noise ($K_{\text{true}} = 10$, $\sigma_y = 0.2$): Despite heavy noise, the physics-informed prior maintains stability. The red dotted line represents the true time to reach 99% saturation.

TABLE III. Comparison of targeted vs. measured saturation levels and prediction error

Targeted Saturation (%)	Pulse Time (s)	GPC (nm)	Measured Saturation (%)	Error (%)
95	5.217	0.0425	94.4	0.6
90	2.471	0.0378	84.0	6.8
85	1.556	0.0345	76.7	9.8
80	1.098	0.0313	69.6	13.0

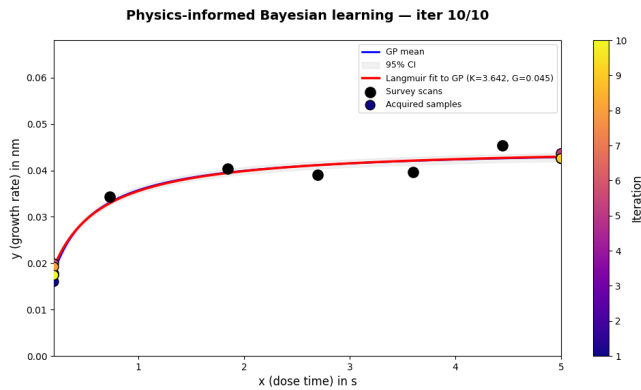


FIG. 11. Distribution of sampled points across iterations during the experimental validation of TDMAT/O₃ ALD. The Bayesian framework concentrates sampling in the high-saturation regime and steep-slope region while utilizing survey points for mid-range coverage. Colors indicate iteration number.

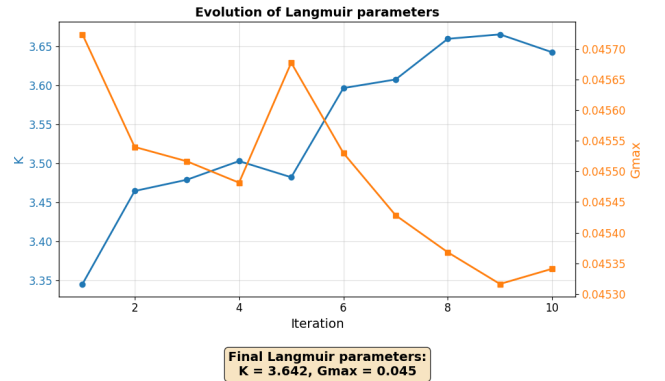


FIG. 12. Experimental results showing the evolution of Langmuir parameters K and G_{max} across active learning iterations. Both parameters demonstrate stable convergence, validating the two-stage parameter estimation strategy.

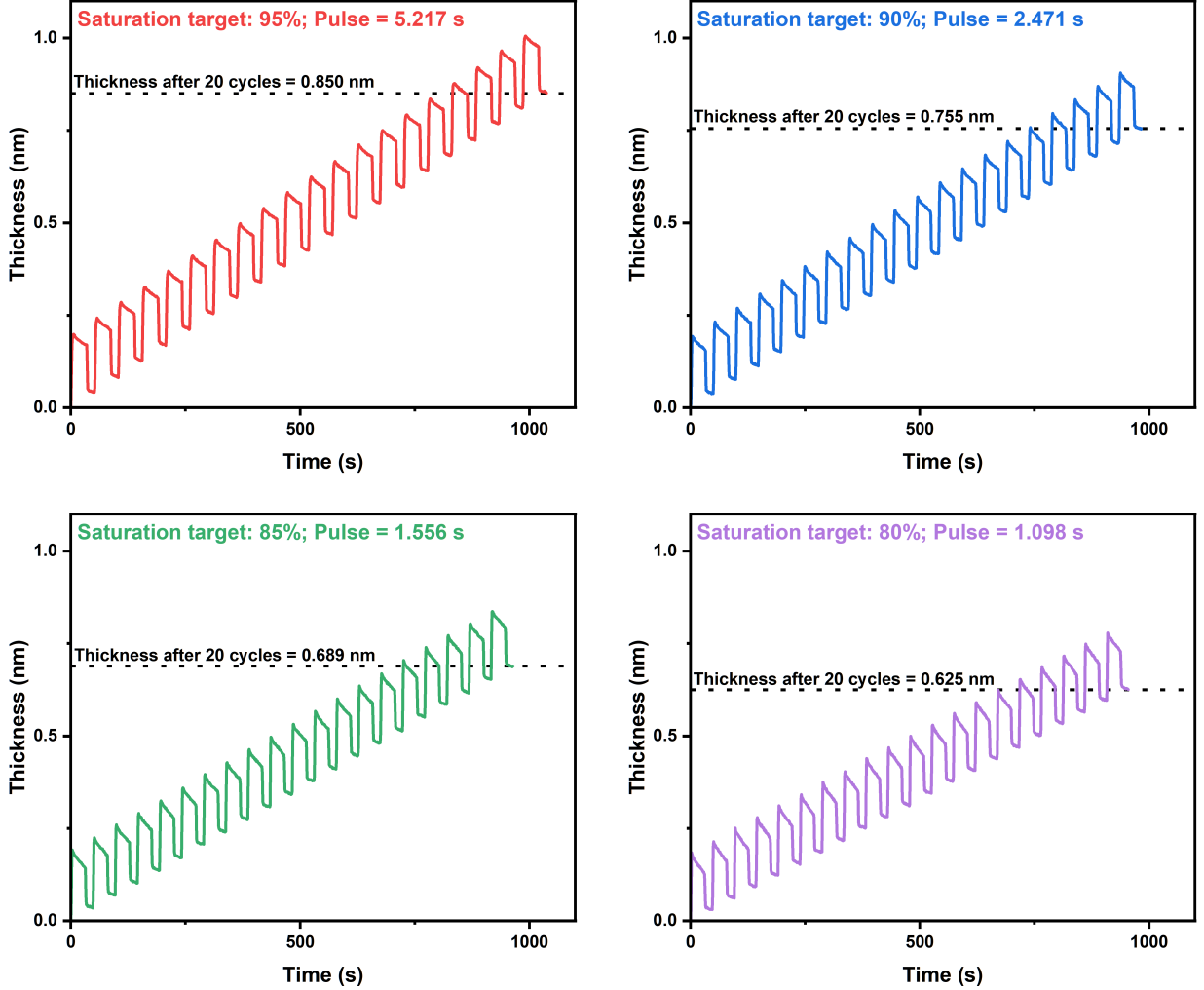


FIG. 13. Accuracy assessment of predicted saturation times. The plots show the growth over 20 cycles for four different pulse times: **Red** 95% saturation (5.217 s, GPC = 0.0425 nm), **Blue** 90% saturation (2.471 s, GPC = 0.0378 nm), **Green** 85% saturation (1.556 s, GPC = 0.0345 nm), and **Purple** 80% saturation (1.098 s, GPC = 0.0313 nm). The maximum GPC (G_{\max}) is 0.045 nm. While the model accurately predicts high saturation targets (95%), deviations increase at lower targets due to non-ideal desorption effects.

larger relative loss when equilibrium within the cycles is not achieved. This behavior is consistent with the non-ideal kinetics expected in real ALD systems and highlights the importance of considering alternative kinetic models when targeting intermediate and low coverage regimes.

V. CONCLUSION

We have demonstrated a physics-informed BAL framework that significantly accelerates the determination of saturation pulse times in ALD. By embedding the Langmuir isotherm, the most widely accepted and fundamental model for ALD saturation behavior directly into the covariance kernel and utilizing a GP-smoothed parameter estimation technique, the model achieves rapid convergence even in the presence of

significant measurement noise and timing jitter. The primary goal of this work is to establish a robust active learning framework rather than to develop comprehensive kinetic models. Our simulations reveal three key advantages over standard data-driven approaches: **Efficiency:** The physics-informed model consistently identifies target saturation times within five iterations, while reducing precursor consumption by up to 75%. **Extrapolation:** Unlike standard GPs, which struggle at the boundaries of the search space, the Langmuir-transformed kernel enables accurate extrapolation to saturation times beyond the explored experimental window. **Robustness:** The two-stage fitting strategy effectively filters experimental noise, maintaining high predictive accuracy even when signal degradation occurs.

Experimental validation using TDMAT/ O_3 deposition confirms the practical utility of the framework. The model suc-

cessfully identified saturation times for high-coverage targets ($\geq 95\%$) with less than 1% error, validating its effectiveness for practical optimization. Our experimental observations reveal that while the Langmuir model captures the general saturation trend, it may not fully represent the true kinetics, particularly in low-saturation regimes where deviations become apparent. Despite these deviations, the framework demonstrates reliable performance for practical optimization tasks.

We recognize that a more sophisticated kinetic model (potentially incorporating more than two adjustable parameters) would better describe both classical Langmuir behavior and non-ideal low-saturation regimes. However, such a study requires extensive experimental characterization and mechanistic investigation of adsorption-desorption behaviors, which falls outside the scope of this work. To maintain focus on the active learning algorithm and its practical implementation, we defer this detailed kinetic analysis to future studies. We are currently conducting in-depth experimental characterization to develop such a model specialized to be used in our framework, which will be published separately. Importantly, the provided open-source code is modular and easily adaptable, allowing researchers to implement alternative kinetic models tailored to their specific ALD systems. This methodology provides a generalizable, sample-efficient strategy for ALD process development, offering a rigorous path toward autonomous, closed-loop tuning in experimental reactor environments.

ACKNOWLEDGMENTS

The authors acknowledge financial support from University of Illinois Chicago Department of Biomedical Engineering.

DATA AVAILABILITY STATEMENT

Python implementation code for the physics-informed Bayesian active learning framework is provided in the Supporting Information. Additional data including raw experimental measurements are available upon request from the corresponding author.

- ¹S. M. George, "Atomic Layer Deposition: An Overview," *Chem. Rev.* **110**, 111–131 (2010).
- ²S. E. Kim, J. Y. Sung, Y. Yun, B. Jeon, S. M. Moon, H. B. Lee, C. H. Lee, H. J. Jung, J.-U. Lee, and S. W. Lee, "Atomic layer deposition of high- k and metal thin films for high-performance DRAM capacitors: A brief review," *Current Applied Physics* **64**, 8–15 (2024).
- ³T. Gougousi, "Atomic layer deposition of high- k dielectrics on III–V semiconductor surfaces," *Progress in Crystal Growth and Characterization of Materials Special Issue: Recent Progress on Fundamentals and Applications of Crystal Growth; Proceedings of the 16th International Summer School on Crystal Growth (ISSCG-16)*, **62**, 1–21 (2016).
- ⁴J. Sheng, J.-H. Lee, W.-H. Choi, T. Hong, M. Kim, and J.-S. Park, "Review Article: Atomic layer deposition for oxide semiconductor thin film transistors: Advances in research and development," *J. Vac. Sci. Technol. A* **36**, 060801 (2018).
- ⁵A. Lan, H. Lu, B. Huang, F. Chen, Z. Chen, J. Wang, L. Li, and H. Do, "Toward Commercial-Scale Perovskite Solar Cells: The Role of ALD-SnO₂ Buffer Layers in Performance and Stability," *ACS Appl. Mater. Interfaces* **16**, 64825–64833 (2024).

- ⁶S. Seo, S. Jeong, H. Park, H. Shin, and N.-G. Park, "Atomic layer deposition for efficient and stable perovskite solar cells," *Chem. Commun.* **55**, 2403–2416 (2019).
- ⁷M. A. Hossain, K. T. Khoo, X. Cui, G. K. Poduval, T. Zhang, X. Li, W. M. Li, and B. Hoex, "Atomic layer deposition enabling higher efficiency solar cells: A review," *Nano Materials Science Special Issue on Nanostructured Materials for Energy Conversion and Storage*, **2**, 204–226 (2020).
- ⁸S. Hashemi Astaneh, L. P. Faverani, C. Sukotjo, and C. G. Takoudis, "Atomic layer deposition on dental materials: Processing conditions and surface functionalization to improve physical, chemical, and clinical properties - A review," *Acta Biomaterialia* **121**, 103–118 (2021).
- ⁹M. Weber, N. Boysen, O. Graniel, A. Sekkat, C. Dussarrat, P. Wiff, A. Devi, and D. Muñoz-Rojas, "Assessing the Environmental Impact of Atomic Layer Deposition (ALD) Processes and Pathways to Lower It," *ACS Mater. Au* **3**, 274–298 (2023).
- ¹⁰P. Navabi, R. Ampadi Ramachandran, H. Bhatia, M. Jaber-Douraki, U. Diwekar, C. Sukotjo, and C. G. Takoudis, "Artificial intelligence in atomic layer deposition," *J. Vac. Sci. Technol. A* **43**, 060801 (2025).
- ¹¹A. Arunachalam, S. N. Berriel, C. Feit, U. Kumar, S. Seal, K. Basu, and P. Banerjee, "Machine learning approach to thickness prediction from in situ spectroscopic ellipsometry data for atomic layer deposition processes," *J. Vac. Sci. Technol. A* **40**, 012405 (2021).
- ¹²A. Yanguas-Gil and J. W. Elam, "Machine learning and atomic layer deposition: Predicting saturation times from reactor growth profiles using artificial neural networks," *J. Vac. Sci. Technol. A* **40**, 062408 (2022).
- ¹³M. Tom, H. Wang, F. Ou, G. Orkoulas, and P. D. Christofides, "Machine Learning Modeling and Run-to-Run Control of an Area-Selective Atomic Layer Deposition Spatial Reactor," *Coatings* **14**, 38 (2024).
- ¹⁴Y. Ding, Y. Zhang, H. Y. Chung, and P. D. Christofides, "Machine learning-based modeling and operation of plasma-enhanced atomic layer deposition of hafnium oxide thin films," *Computers & Chemical Engineering* **144**, 107148 (2021).
- ¹⁵G. Dogan, S. O. Demir, R. Gutzler, H. Gruhn, C. B. Dayan, U. T. Sanli, C. Silber, U. Culha, M. Sitti, G. Schütz, C. Grévent, and K. Keskinbora, "Bayesian Machine Learning for Efficient Minimization of Defects in ALD Passivation Layers," *ACS Appl. Mater. Interfaces* **13**, 54503–54515 (2021).
- ¹⁶P. Häussermann, N. B. Joseph, and D. Hiller, "Leveraging Bayesian Optimization Software for Atomic Layer Deposition: Single-Objective Optimization of TiO₂ Layers," *Materials* **17**, 5019 (2024).
- ¹⁷N. H. Paulson, A. Yanguas-Gil, O. Y. Abuomar, and J. W. Elam, "Intelligent Agents for the Optimization of Atomic Layer Deposition," *ACS Appl. Mater. Interfaces* **13**, 17022–17033 (2021).
- ¹⁸J. Cagnazzo, O. S. Abuomar, A. Yanguas-Gil, and J. W. Elam, "Atomic Layer Deposition Optimization Using Convolutional Neural Networks," in *2021 International Conference on Computational Science and Computational Intelligence (CSCI)* (2021) pp. 228–232.
- ¹⁹P. Häussermann, N. B. Joseph, and D. Hiller, "Leveraging Bayesian Optimization Software for Atomic Layer Deposition: Single-Objective Optimization of TiO₂ Layers," *Materials* **17**, 5019 (2024).
- ²⁰A. Yanguas-Gil, S. Letourneau, N. Paulson, and J. W. Elam, "Experimental platform and digital twin for AI-driven materials optimization and discovery for microelectronics using atomic layer deposition," in *AI for Accelerated Materials Design NeurIPS 2022 Workshop* (2022).
- ²¹I. Sekulic, J. Schaible, G. Müller, M. Plock, S. Burger, V. J. Martínez-Lahuerta, N. Gaaloul, and P.-I. Schneider, "Physics-informed Bayesian optimization of expensive-to-evaluate black-box functions," *Mach. Learn.: Sci. Technol.* **6**, 040503 (2025).
- ²²D. Khatamsaz, R. Neuberger, A. M. Roy, S. H. Zadeh, R. Otis, and R. Arroyave, "A physics informed bayesian optimization approach for material design: Application to NiTi shape memory alloys," *npj Comput Mater* **9**, 221 (2023).
- ²³V. Ladygin, I. Beniya, E. Makarov, and A. Shapeev, "Bayesian learning of the thermodynamic integration and numerical convergence for accurate phase diagrams," *Phys. Rev. B* **104**, 104102 (2021).
- ²⁴I. A. Bernalov, N. V. Krivoschapov, A. A. Lisov, V. A. Chaliy, and M. G. Medvedev, "Physics-Informed Bayesian Optimization for Conformational Ensemble Augmentation," *J. Chem. Inf. Model.* **65**, 6048–6056 (2025).
- ²⁵J. Dendooven, D. Deduytsche, J. Musschoot, R. L. Vanmeirhaeghe, and C. Detavernier, "Modeling the Conformality of Atomic Layer Deposition: The Effect of Sticking Probability," *J. Electrochem. Soc.* **156**, P63 (2009).

- ²⁶A. Yanguas-Gil and J. W. Elam, "Simple model for atomic layer deposition precursor reaction and transport in a viscous-flow tubular reactor," *J. Vac. Sci. Technol. A* **30**, 01A159 (2011).
- ²⁷T. Muneshwar and K. Cadien, "Surface reaction kinetics in atomic layer deposition: An analytical model and experiments," *J. Appl. Phys.* **124**, 095302 (2018).
- ²⁸C. E. Rasmussen and C. K. I. Williams, *Gaussian Processes for Machine Learning*.
- ²⁹V. L. Deringer, A. P. Bartók, N. Bernstein, D. M. Wilkins, M. Ceriotti, and G. Csányi, "Gaussian Process Regression for Materials and Molecules," *Chem. Rev.* **121**, 10073–10141 (2021).
- ³⁰F. Pedregosa, G. Varoquaux, A. Gramfort, V. Michel, B. Thirion, O. Grisel, M. Blondel, P. Prettenhofer, R. Weiss, V. Dubourg, J. Vanderplas, A. Passos, D. Cournapeau, M. Brucher, M. Perrot, and É. Duchesnay, "Scikit-learn: Machine learning in python," *Journal of Machine Learning Research* **12**, 2825–2830 (2011).
- ³¹P. Virtanen, R. Gommers, T. E. Oliphant, M. Haberland, T. Reddy, D. Cournapeau, E. Burovski, P. Peterson, W. Weckesser, J. Bright, S. J. van der Walt, M. Brett, J. Wilson, K. J. Millman, N. Mayorov, A. R. J. Nelson, E. Jones, R. Kern, E. Larson, C. J. Carey, Í. Polat, Y. Feng, E. W. Moore, J. VanderPlas, D. Laxalde, J. Perktold, R. Cimrman, I. Henriksen, E. A. Quintero, C. R. Harris, A. M. Archibald, A. H. Ribeiro, F. Pedregosa, and P. van Mulbregt, "SciPy 1.0: Fundamental algorithms for scientific computing in Python," *Nat Methods* **17**, 261–272 (2020).
- ³²J. Snoek, H. Larochelle, and R. P. Adams, "Practical bayesian optimization of machine learning algorithms," in *Advances in Neural Information Processing Systems*, Vol. 25, edited by F. Pereira, C. Burges, L. Bottou, and K. Weinberger (Curran Associates, Inc., 2012).
- ³³Y.-W. Kim and D.-H. Kim, "Atomic layer deposition of TiO₂ from tetrakisdimethylamido-titanium and ozone," *Korean J. Chem. Eng.* **29**, 969–973 (2012).